

# $\pi\pi$ scattering in the $\rho$ -meson channel at finite temperature

Y. B. He, J. Hübner, S. P. Klevansky, and P. Rehberg

*Institut für Theoretische Physik,*

*Philosophenweg 19, D-69120 Heidelberg, Germany*

## Abstract

We study  $\pi\pi$  scattering in the  $I = 1$ ,  $J^P = 1^-$  channel at finite temperature in the framework of the extended Nambu-Jona-Lasinio model that explicitly includes vector and axial-vector degrees of freedom in addition to the usual scalar and pseudoscalar sector. The  $S$ -matrix in the coupled channels  $q\bar{q}$  and  $\pi\pi$  is constructed via  $\rho$ -exchange in the  $s$ -channel. The self-energy of the  $\rho$ -meson contains both quark and pion loop contributions. The analytic structure of the  $S$ -matrix for  $T \geq 0$  is investigated and the motion of the  $\rho$ -pole as a function of coupling constant and temperature is followed in the complex  $\sqrt{s}$ -plane. For numerical calculations, parameters are chosen in order that  $m_\pi$ ,  $f_\pi$  and the experimental  $\pi\pi$  phase shifts  $\delta_1^1$  at zero temperature are reproduced, and then the behavior of the  $\rho$ -pole as well as the  $\pi\pi$  cross section is investigated as a function of the temperature. We find that the position of the  $\rho$  mass stays practically constant for  $0 \leq T \leq 130$  MeV, and then moves down in energy by about 200 MeV for  $130 \text{ MeV} \leq T \leq 230$  MeV.

25.75.-q, 12.39.Ba, 21.65.+f, 24.85.+p

**Keywords:**  $\pi\pi$  scattering,  $\rho$ -meson, finite temperature, analytic structure.

Typeset using REVTeX

## I. INTRODUCTION

During the last decade many experimental and theoretical efforts have been dedicated to the study of relativistic heavy-ion collisions, in which one hopes to observe the two aspects of the QCD phase transition: (i) the confinement / deconfinement transition in which hadronic matter decomposes into the quark-gluon plasma, and the converse process, and (ii) that of chiral symmetry restoration / breaking, both of which should occur at high values of the temperature and / or density. Depending on the energy density reached, the hot fireball formed after the collisions may (or may not) enter into the quark-gluon plasma phase and undergo a chiral transition simultaneously before it cools down and hadronizes, leaving it a challenge for people to identify its trajectory from the observed hadronic products. In particular, during the evolution of the fireball, a large number of pions is produced in the mid-rapidity region, and one can expect that interactions between them play an essential role in the dynamical evolution. It is thus of interest to study the  $\pi\pi$  scattering in a thermal environment in order to understand the evolution dynamics of the system. The  $\pi\pi$  scattering cross section, for example, is an important input to transport equations that are used to simulate the dynamical evolution of the fireball. Based on hadronic models, Refs. [1,2] have investigated the  $\pi\pi$  cross section in nuclear matter, and have claimed to observe considerable medium effects. In itself, a study of the temperature dependence of the  $\pi\pi$  scattering cross section is necessary, and we will examine this here in the framework of a chiral model. On the other hand,  $\pi\pi$  annihilation is one important source of dilepton production. In recent studies by the CERES and HELIOS-3 collaborations [3], an enhancement of the dilepton spectrum has been observed in the energy range of 200 - 800 MeV in nucleus-nucleus collisions. One of the hypotheses brought forward to explain these data is that the  $\rho$ -meson mass shifts to lower values as a function of increasing temperature and density, and its width broadens while doing so [4]. Since a major source of dileptons in this energy range comes from the  $\rho$ -meson, it is necessary to understand to what extent a mass shift can occur, and if one occurs, whether it is an increase or decrease. Thus, via our study of the  $\pi\pi$  system, we also wish to examine the medium dependence of the  $\rho$ -meson. These two problems, that of  $\pi\pi$  scattering at energies  $500 \text{ MeV} < \sqrt{s} < 900 \text{ MeV}$  and that of the medium dependence of the  $\rho$ -meson, are

closely intertwined, and we address both of these problems in this paper.

The medium effects of the  $\rho$ -meson have been extensively discussed recently and for a review we refer the reader to Ref. [5]. The  $\rho$ -meson properties at finite temperature are not yet well understood, and in particular the issue as to whether the  $\rho$  mass increases or decreases with increasing temperature has not yet been settled [6–9]. In Ref. [6], for example, a vector dominance model that does not support a chiral or deconfinement phase transition is used to describe the temperature dependence, and these authors find a weak rising temperature dependence of the  $\rho$  mass and width. On the other hand, recent lattice calculations have found no sign of a temperature dependence in the meson properties for temperatures up to  $0.92T_c$  [10]. In this work, we study the temperature dependence within a chiral model that displays a phase transition in the chiral limit and a smooth crossover for small values of the current quark mass. We investigate the analytic structure of the  $\rho$  propagator and consider the  $\rho$ -meson as a pole in the complex plane. In this way we contribute additional insight.

Our starting point is an effective chiral model: we use a version of the Nambu-Jona-Lasinio (NJL) model [11,12] that has been extended to explicitly include vector and axial-vector degrees of freedom [13–15] in order to study the  $\pi\pi$  cross section at finite temperature and vanishing chemical potential under inclusion of the  $\rho$ -meson. The NJL-model, constructed essentially on the observation of the chiral symmetry of quantum chromodynamics (QCD) gives a transparent description of the mechanism of spontaneous symmetry breaking. It has been extensively used to study the static meson properties, and has enjoyed remarkable success, especially in the pseudoscalar sector [11,12]. However, to describe the  $\rho$ -meson in the context of the NJL-model is a delicate task [16,17], since, on heuristic grounds,  $m_\rho \simeq 2m_q$ , where  $m_q \sim 300\text{--}400$  MeV is the mass of the constituent quark, and the NJL-model does not confine quarks. In the language of scattering theory, the  $\rho$  mass is close to the  $q\bar{q}$  threshold. While threshold effects often modify the shape of a resonance on the real energy axis close by, the position of a pole in the complex plane is much less distorted. For this reason we choose to define the properties of the  $\rho$ -meson as those of the pole in the complex plane. The self-energy of the  $\rho$ -meson in the NJL-model arises from the quark loop contribution at the lowest order in an expansion in the inverse number of colors,  $1/N_c$ , which leads to the unphysical decay  $\rho \rightarrow q\bar{q}$  that is

due to the lack of confinement.<sup>1</sup> On the other hand, it is known from experiment that almost all  $\rho$ -mesons decay via the channel  $\rho \rightarrow \pi\pi$ , and thus a satisfactory description of the  $\rho$ -meson cannot be obtained unless the physical  $\rho$ -meson decay channel has been taken into account. From the point of view of the NJL model, the necessary pion loop corrections can be classified as part of the next order in the  $1/N_c$  expansion [19,20]. In fact, these terms should represent the leading contributions at this order [21]. It is also necessary to include the pion loop contribution to the  $\rho$ -meson self-energy in order to fulfill the unitarity of the  $\pi\pi$  scattering amplitude. With the inclusion of both pion loop and quark loop contributions to the  $\rho$ -meson self-energy, the  $\pi\pi$  scattering via  $\rho$ -meson exchange becomes a coupled channel (*i.e.*  $\pi\pi$  and  $q\bar{q}$  channels) process. Care has to be taken to obey current conservation. We study the analytic structure of the  $\rho$ -meson propagator or scattering amplitude in the complex energy plane, in order to identify the  $\rho$  mass as a pole. This part of the work is completely new. The parameters of the model can be chosen such that at  $T = 0$ , the values of  $m_\pi$ ,  $f_\pi$  and the experimental data of the  $\pi\pi$  phase shifts are well reproduced. Temperature effects are incorporated via the imaginary time formalism and the temperature dependence of the  $\pi\pi$  cross section is obtained. Note that  $\pi\pi$  scattering has been studied by several authors in the context of the NJL model, however only to obtain the scattering lengths at zero temperature without the inclusion of the vector meson sector [22], and also with it [23]. Scattering lengths at finite temperature were calculated in [24].

One may well ask the question as to the validity of the NJL model in describing the  $\rho$ -meson in the manner described. No conceptual difficulty arises with the cutoff. It restricts the three momentum  $|\vec{p}| < \Lambda$  and there is no condition on the mass. The problem lies rather in the fact that the unphysical  $\rho \rightarrow q\bar{q}$  channel is open, and the poles of the propagator, if taken only in the lowest order in the  $1/N_c$  expansion, will only reflect this physics. In spite of this, several authors [18,15] have found that the static properties in the vector meson sector can still be well understood, and that this model can still be used in a range which may *a priori* seem to lie outside of its realm of validity. Although we have gone beyond this restrictive approximation

---

<sup>1</sup>In spite of this deficiency, this model still appears to give a good description of the position of the  $\rho$ -mass [18,15].

allowing in addition the physical decay channel  $\rho \rightarrow \pi\pi$  to open, we are still able to observe and isolate the effects of the opening of the unphysical  $q\bar{q}$  threshold. This can be clearly seen in the calculated  $\pi\pi$  cross section, and is discussed at that point.

This paper is organized as follows. In Sec. II, we describe our formalism in the context of an extended NJL-model for mesons as quark-antiquark excitations, and calculate the vector and pseudoscalar mesonic modes that correspond to the  $\rho$ -meson and  $\pi$ -meson. We then calculate the  $\rho\pi\pi$  vertex which is an important element in the pion loop correction and also for  $\pi\pi$  scattering. The physical process  $\rho \rightarrow \pi\pi$  is then incorporated into the  $\rho$ -meson self-energy as a higher order correction in the inverse number of colors  $1/N_c$  in the NJL model. The calculations of  $\pi\pi$  scattering amplitude and cross section are outlined in Sec. III. Numerical results are presented in Sec. IV, where we show the variations of the position of the  $\rho$ -pole with coupling strength and temperature, and the temperature dependence of the  $\pi\pi$  cross section. In Sec. V, we summarize our results and their implications. Some calculations of quark loop contribution to the self-energy of different mesonic modes are collected in Appendix A.

## II. MESONS IN THE EXTENDED NAMBU-JONA-LASINIO MODEL

Our starting point is the extended two-flavor Nambu-Jona-Lasinio Lagrangian density:

$$\begin{aligned} \mathcal{L} = & \bar{\psi} (i\rlap{\not{D}} - m_0)\psi + G_1 \left[ (\bar{\psi}\psi)^2 + (\bar{\psi}i\gamma_5\tau^a\psi)^2 \right] \\ & - G_2 \left[ (\bar{\psi}\gamma^\mu\tau^a\psi)^2 + (\bar{\psi}\gamma^\mu\gamma_5\tau^a\psi)^2 \right], \end{aligned} \quad (2.1)$$

with the spinors  $\psi$  in Dirac, color and flavor space, and  $m_0$  a small common current mass for the up and down quarks,  $m_0^u = m_0^d = m_0$ . The  $\tau^a$ ,  $a = 1, 2, 3$ , represent the isospin Pauli matrices, and  $G_1$  and  $G_2$  are coupling constants of dimension  $[\text{Mass}]^{-2}$ . Eq. (2.1) is an extended version of the original NJL model which also includes terms associated with the vector and axial-vector meson modes. In the chiral limit,  $m_0 = 0$ , this Lagrangian displays  $SU_L(2) \otimes SU_R(2)$  chiral symmetry even for different coupling constants  $G_1$  and  $G_2$  in the scalar-pseudoscalar and vector-axial-vector sectors. The NJL model is not a renormalizable field theory due to the fact that the interaction between quarks is assumed to be point-like. It is therefore necessary

to specify a regularization scheme in order to define the NJL model completely. Throughout this work, we shall employ a three-momentum cutoff scheme in which we introduce a parameter  $\Lambda$ , such that  $p < \Lambda$ . This cutoff  $\Lambda$ , together with  $m_0$ ,  $G_1$  and  $G_2$ , are the four parameters in our present model. Note that this Lagrangian has already been studied in detail elsewhere [13,15,17]. We follow the notation of Ref. [15] and refer the reader to this paper for extensive detail. Therefore in the following subsections, we only present those details which we directly require for the calculations of the  $\pi\pi$  scattering in the  $\rho$ -meson channel.

### A. Mesons as quark-antiquark excitations

Mesons as  $q\bar{q}$  bound states or resonances can be obtained from the quark-antiquark scattering amplitude. For example, in the present model, there are collective modes carrying the quantum numbers  $J^{PC} = 0^{-+}, 0^{++}, 1^{--}$ , and  $1^{++}$  that are composed of interacting  $q\bar{q}$  pairs, and which have the same quantum numbers as the  $\pi$ ,  $\sigma$ ,  $\rho$ , and  $a_1$  mesons. For brevity, we shall refer to these modes as meson states of the corresponding name in the following discussions.

For our purpose of studying  $\pi\pi$  scattering, we require the effective propagators of the  $\pi$  and  $\rho$ -mesons, as well as the effective vertex of the  $\pi q\bar{q}$  interaction, all of which can be found by constructing the quark-antiquark scattering amplitude. We list these results here first.

Consider first the vector meson exchange channel, since in the present model, this channel is simplest as it does not couple with other channels. In the random phase approximation, the quark-antiquark scattering amplitude shown in Fig. 1 can be expressed to leading order in  $1/N_c$  as an infinite sum of quark-loop chains, and can also be recast into the form of a Schwinger-Dyson equation. The  $\rho$ -meson exchange amplitude  $D_{ab}^{\mu\nu}(q^2)$  for quark-antiquark scattering can be generated by the one-loop polarization function  $\Pi_{\mu\nu,ab}^{VV}(q^2)$  via the Schwinger-Dyson equation of Fig. 1,

$$[-iD_{ab}^{\mu\nu}] = [-2iG_2\delta_{ab}g^{\mu\nu}] + [-2iG_2\delta_{ac}g^{\mu\lambda}] [-i\Pi_{\lambda\sigma,cd}^{VV}] [-iD_{db}^{\sigma\nu}], \quad (2.2)$$

where  $a, b, c, d$  are isospin indices, and  $\mu, \nu$  Lorentz indices. The notation  $VV$  refers to the vector-vector channel. The calculation of the one-loop polarization function  $\Pi_{\mu\nu,ab}^{VV}(q^2)$  is straightforward [15], and is collected for completeness in the Appendix

together with some other one-loop polarization functions for different channels that we need in the calculations below. The Lorentz and flavor structure for the  $\rho$ -meson channel allows for the decomposition into transverse ( $T$ ) and longitudinal ( $L$ ) components, *i.e.*

$$\Pi_{\mu\nu,ab}^{VV}(q^2) = [\Pi_T^{VV}(q^2)T_{\mu\nu} + \Pi_L^{VV}(q^2)L_{\mu\nu}] \delta_{ab}, \quad (2.3)$$

where  $L^{\mu\nu} = \hat{q}^\mu \hat{q}^\nu$  and  $T^{\mu\nu} = g^{\mu\nu} - \hat{q}^\mu \hat{q}^\nu$  with  $\hat{q}^\mu = q^\mu / \sqrt{q^2}$ . Consequently the  $\rho$ -meson exchange amplitude can also be decomposed into transverse and longitudinal components as

$$D_{ab}^{\mu\nu}(q^2) = [D_T(q^2)T^{\mu\nu} + D_L(q^2)L^{\mu\nu}] \delta_{ab}, \quad (2.4)$$

where

$$-iD_{T,L}(q^2) = \frac{-2iG_2}{1 + 2G_2\Pi_{T,L}^{VV}(q^2)}. \quad (2.5)$$

It will be seen later that only the transverse exchange amplitude of the  $\rho$ -meson enters into the  $\pi\pi$  scattering amplitude.

In the pion channel, the situation is more complicated because of the mixing between the pseudoscalar ( $\pi$ ) and axial-vector ( $a_1$ ) channels. In analogy to the case in the  $\rho$ -meson channel, the Lorentz and flavor structure of the relevant one-loop polarizations [15] (see the Appendix) leads to the following decompositions,

$$D_{\mu\nu,ab}^{AA}(q^2) = [D_T^{AA}(q^2)T_{\mu\nu} + D_L^{AA}(q^2)L_{\mu\nu}] \delta_{ab} \quad (2.6)$$

$$D_{\mu,ab}^{AP}(q^2) = D^{AP}(q^2)\hat{q}_\mu \delta_{ab}, \quad (2.7)$$

$$D_{\mu,ab}^{PA}(q^2) = D^{PA}(q^2)\hat{q}_\mu \delta_{ab}, \quad (2.8)$$

$$D_{ab}^{PP}(q^2) = D^{PP}(q^2)\delta_{ab}, \quad (2.9)$$

where the indices  $A$  and  $P$  refer to the axial and pseudoscalar channels, respectively. The Schwinger-Dyson equations become a set of coupled equations that can be written in matrix form as

$$-i\mathbf{D} = i\mathbf{K} + i\mathbf{K}[-i\mathbf{\Pi}][-i\mathbf{D}], \quad (2.10)$$

where

$$-i\mathbf{D} = \begin{pmatrix} -iD^{PP} & -iD^{PA} \\ -iD^{AP} & -iD_L^{AA} \end{pmatrix}, \quad \mathbf{K} = \begin{pmatrix} 2G_1 & 0 \\ 0 & -2G_2 \end{pmatrix}. \quad (2.11)$$

This matrix equation has the solution

$$\begin{aligned} -i\mathbf{D} &= i\mathbf{K}(\mathbf{1} - \mathbf{\Pi K})^{-1} \\ &= \frac{2iG_1}{\mathcal{D}} \begin{pmatrix} A & iB \\ -iB & C \end{pmatrix}, \end{aligned} \quad (2.12)$$

where  $A = 1 + 2G_2\Pi_L^{AA}$ ,  $B = 2iG_2\Pi^{PA}$ ,  $C = -G_2(1 - 2G_1\Pi^{PP})/G_1$ , and  $\mathcal{D} = \text{Det}(\mathbf{1} - \mathbf{\Pi K})$ .

In order to resolve the mixing between pseudoscalar and axial-vector modes and identify the corresponding independent eigenstates and their coupling to the quarks, the matrix of the coupled exchange amplitudes which appears in the quark-antiquark scattering amplitude,

$$-i\mathcal{T} = (i\gamma_5\tau, \quad \gamma_\mu\gamma_5\tau) \begin{pmatrix} -iD^{PP} & -iD^{PA}\hat{q}_\nu \\ -iD^{AP}\hat{q}_\mu & -iD_L^{AA}L_{\mu\nu} \end{pmatrix} \begin{pmatrix} i\gamma_5\tau \\ \gamma^\nu\gamma_5\tau \end{pmatrix}, \quad (2.13)$$

has to be diagonalized. One obtains the form

$$-i\mathcal{T} = -i\mathcal{T}_\pi - i\mathcal{T}_a, \quad (2.14)$$

with  $-i\mathcal{T}_\pi$  and  $-i\mathcal{T}_a$  being the  $q\bar{q}$  scattering amplitudes for the pure pseudoscalar ( $\pi$ ) and axial-vector ( $a_1$ ) exchange, respectively. For our purpose, we examine only  $-i\mathcal{T}_\pi$  and approximate it near the pole position as

$$-i\mathcal{T}_\pi \sim [(ig_{\pi qq} - ig_{pv}\frac{\not{q}}{2m_q})i\gamma_5\tau] \otimes [(ig_{\pi qq} + ig_{pv}\frac{\not{q}}{2m_q})i\gamma_5\tau] \frac{i}{q^2 - m_\pi^2}, \quad (2.15)$$

from which we can read off the complete  $\pi q\bar{q}$  vertex to be

$$(ig_{\pi qq} - ig_{pv}\frac{\not{q}}{2m_q})i\gamma_5\tau. \quad (2.16)$$

In this expression, the relevant coupling constants  $g_{\pi qq}$  and  $g_{pv}$  are given as

$$g_{\pi qq}^2 = -2G_1(1 + 2G_2\Pi_L^{AA}) \left( \frac{\partial\mathcal{D}(q^2)}{\partial q^2} \right)^{-1} \Bigg|_{q^2=m_\pi^2}, \quad (2.17)$$

and



$$g_{pv}^2 = 2G_2(1 - 2G_1\Pi^{PP}) \left( \frac{4m_q^2}{q^2} \right) \left( \frac{\partial\mathcal{D}(q^2)}{\partial q^2} \right)^{-1} \Big|_{q^2=m_\pi^2}. \quad (2.18)$$

The additional pseudovector coupling constant  $g_{pv}$  is induced by the pseudoscalar-axial-vector mixing [13].

Note that in this section, our formulae have been explicitly stated for temperature  $T = 0$ . The generalization to finite temperature leaves these equations formally unaltered - in that case, however, Lorentz invariance is broken and the functions are no longer a function of  $q^2$ , rather of  $q_0^2$  and  $\vec{q}^2$  separately. The derivatives required in Eqs.(2.17) and (2.18) are then to be taken with respect to  $q_0^2$  and evaluated at  $q_0^2 = m_\pi^2$ , and  $\mathbf{q}^2 = 0$ . However, in the following, for brevity we will still use 4-momentum argument in the expressions even for finite temperature, and they should be understood in the above sense.

### B. $\rho\pi\pi$ vertex

The  $\rho\pi\pi$  vertex is an essential element which is required for constructing the pion loop graph and the  $\pi\pi$  scattering amplitude. As will be seen in the next subsection, the  $\rho$ -meson may couple to pions via a triangular quark loop which is shown in Fig. 2. Using Feymann rules for finite temperature, one may write

$$\begin{aligned} -i\Gamma_\mu^{\rho\pi\pi}(p', p) = & 2 \times (-1) \times \frac{i}{\beta} \sum_n \int^\Lambda \frac{d^3k}{(2\pi)^3} \text{Tr}[(ig_{\pi qq} + ig_{pv} \frac{\not{p}}{2m_q})i\gamma_5 iS(k) \\ & \times (ig_{\pi qq} - ig_{pv} \frac{\not{p}'}{2m_q})i\gamma_5 iS(p' + k)\gamma_\mu iS(p + k)], \end{aligned} \quad (2.19)$$

where the trace  $\text{Tr}[\dots]$  is to be carried out over the color and spinor indices,  $\beta$  is the inverse temperature, and the Matsubara sum in  $n$  runs over the fermionic frequencies  $\omega_n = (2n + 1)\pi/\beta$ , with  $n = 0, \pm 1, \pm 2, \dots$ , which via  $k = (i\omega_n, \mathbf{k})$  enter into the quark propagator  $S(k)$ . Note that the  $\rho q\bar{q}$  vertex is represented in Eq. (2.19) only in its spinor structure  $\gamma_\mu$ . The coupling strength  $g_{\rho q\bar{q}}$  will always be included via the  $\rho$ -meson exchange amplitude into the scattering amplitude, which is our convention. In deriving Eq. (2.19), we point out that both graphs of Fig. 2 give equal contributions, since they differ from each other for the Dirac trace of the quark loop only by a minus sign, which will be cancelled out by another minus sign arising from the flavor factors. This is the origin of the factor 2 in Eq. (2.19). Note that

the flavor factors have been omitted in Eq. (2.19), and will be incorporated later. We have also introduced the three-momentum cut-off  $\Lambda$  to regularize the divergence of the integral.

Direct evaluation of Eq. (2.19) and an analytic continuation to real variables leads us to the form

$$-i\Gamma_{\mu}^{\rho\pi\pi}(p', p) = -iV_{\rho\pi\pi}(p', p)(p' + p)_{\mu} \quad (2.20)$$

for the vertex, where the dimensionless function  $V_{\rho\pi\pi}$  can be expressed in terms of several elementary integrals  $I_1$ ,  $I_2(p' - p)$ ,  $I_3(p', p)$ , whose definitions are given in Eqs. (A10a)-(A10c) of the Appendix. One finds

$$\begin{aligned} -iV_{\rho\pi\pi}(p', p) = & -4iN_c \{g_{\pi qq}(g_{\pi qq} + g_{pv})I_2(p) \\ & + \frac{(g_{\pi qq} + g_{pv})^2}{q^2 - 4m_{\pi}^2} [(q^2 - 2m_{\pi}^2)[I_2(p' - p) - I_2(p)] + 2m_{\pi}^4 I_3(p', p)] \\ & - \frac{g_{pv}^2}{12m_q^2} [(q^2 + 2m_q^2)I_2(p' - p) - 2I_1] \}, \end{aligned} \quad (2.21)$$

where the momentum of the  $\rho$ -meson is denoted by  $q = p - p'$ , and  $N_c$  is the number of colors.

### C. $1/N_c$ corrections

In this section, we extend the calculation of the  $\rho$ -meson (vector-vector) polarization to the next order in the  $1/N_c$  expansion. There are two types of diagrams that enter at this level, and they are shown as (b) and (c) of Fig. 3, *i.e.* we construct

$$\Pi_{\mu\nu}^{\text{total}} = \Pi_{\mu\nu}^{(q)} + \Pi_{\mu\nu}^{(\pi)} \quad (2.22)$$

where  $\Pi_{\mu\nu}^{(\pi)} = \Pi_{\mu\nu}^{(\pi \text{ loop})} + \Pi_{\mu\nu}^{(\pi \text{ tad})}$ , and  $\Pi_{\mu\nu}^{(\pi \text{ loop})}$  and  $\Pi_{\mu\nu}^{(\pi \text{ tad})}$  refer to the contributions of Fig. 3 (b) and (c), respectively. The function  $\Pi_{\mu\nu}^{(q)}$  refers to the vector-vector polarization of a single quark loop as already introduced in Eq.(2.3),  $\Pi_{\mu\nu}^{(q)} = \Pi_{\mu\nu}^{VV}$ , and which is given in the Appendix, see Eqs.(A11) and (A12). The additional term  $\Pi_{\mu\nu}^{(\pi \text{ loop})}$  that contains the pion loop is necessary on physical grounds, since the decay  $\rho \rightarrow \pi\pi$  is the main decay channel. Within the context of the NJL model, counting arguments in the expansion in powers of  $1/N_c$  allows one to classify this term as being of the next order in  $1/N_c$  relative to the quark bubble. One notes that in addition,

the contribution  $\Pi_{\mu\nu}^{(\pi \text{ tad})}$  is also of the same order. It is required on physical grounds to ensure current conservation [25]. Note that if one were to contract the quark loops of Fig. 3(c) to a point, one would recover the tadpole diagrams of Ref. [6]. We will also see in Sec. III that this choice of diagrams enables us to guarantee unitarity of the  $\pi\pi$  scattering amplitude. With the introduction of this extra contribution, the quark-antiquark scattering amplitude of Eq.(2.5) becomes modified to read

$$-iD_{T,L}(q^2) = \frac{-2iG_2}{1 + 2G_2 [\Pi_{T,L}^{(q)}(q^2) + \Pi_{T,L}^{(\pi)}(q^2)]}. \quad (2.23)$$

In the pole approximation to the pion propagator, the  $\rho$  self-energy arising from the pion loop as shown in Fig. 3(b), is given by:

$$\begin{aligned} -i\Pi_{\mu\nu}^{(\pi \text{ loop})}(q) &= \frac{i}{\beta} \sum_n e^{i\mu_n \eta} \int^\Lambda \frac{d^3p}{(2\pi)^3} [-i\Gamma_\mu^{\rho\pi\pi}(q-p, -p)f_{\rho\pi\pi}] \times [-i\Gamma_\nu^{\rho\pi\pi}(p, p-q)f_{\rho\pi\pi}] \\ &\quad \times \frac{i}{p^2 - m_\pi^2} \times \frac{i}{(q-p)^2 - m_\pi^2}. \end{aligned} \quad (2.24)$$

Here the pion momentum  $p$  is in the imaginary time formalism  $p = (i\mu_n, \mathbf{p})$ , with the bosonic Matsubara frequencies  $\mu_n = 2n\pi/\beta$ ,  $n = 0, \pm 1, \pm 2, \dots$ . After evaluation of the Matsubara sum over  $n$ , the external  $\rho$  momentum  $q = (i\nu_n, \mathbf{q})$  is to be analytically continued to construct a causal propagator,  $m_\pi^2 \rightarrow m_\pi^2 - i\epsilon$ . Due to the complicated structure of the  $\rho\pi\pi$  vertex given in Eq. (2.20), however, the complete calculation of the real part of  $\Pi^{(\pi \text{ loop})}$  is quite difficult. We shall instead approximate in Eq. (2.24) the complete  $[-i\Gamma_\mu(p', p)]$  by  $[-iV_{\rho\pi\pi}(\tilde{p}, \tilde{p})](p+p')_\mu$  with  $\tilde{p} = (q_0/2, \sqrt{q_0^2/4 - m_\pi^2})$ , and  $q_0$  the zeroth component of the  $\rho$  momentum. The  $\rho\pi\pi$  vertex is then independent of the integration variable and can be factored out of the integration. We find the transverse and longitudinal parts of the pion loop contribution to have the form

$$\Pi_T^{(\pi \text{ loop})}(q^2) = -\frac{i}{3} [-iV_{\rho\pi\pi}(\tilde{p}, \tilde{p})f_{\rho\pi\pi}]^2 [(-q^2 + 4m_\pi^2)I_2^{(\pi)}(q) + 2I_1^{(\pi)}], \quad (2.25)$$

$$\Pi_L^{(\pi \text{ loop})}(q^2) = -2i [-iV_{\rho\pi\pi}(\tilde{p}, \tilde{p})f_{\rho\pi\pi}]^2 I_1^{(\pi)}, \quad (2.26)$$

where the integrals  $I_1^{(\pi)}$  and  $I_2^{(\pi)}(p)$  have the same structure as  $I_1$  and  $I_2(p)$  given in Eqs. (A10a) and (A10b) in the Appendix, except that the quark mass  $m$  is to be replaced by the pion mass  $m_\pi$ , and the fermionic frequencies  $\omega_n = (2n+1)\pi/\beta$  are

to be replaced by the bosonic frequencies  $\mu_n = 2n\pi/\beta$  with  $n = 0, \pm 1, \pm 2, \dots$ . An analytic expression for the imaginary part of  $\Pi_T^{(\pi \text{loop})}(q^2)$  can also be derived. One finds

$$\text{Im}\Pi_T^{(\pi \text{loop})}(q^2) = -[-iV_{\rho\pi\pi}(\tilde{p}, \tilde{p})f_{\rho\pi\pi}]^2 \frac{1}{48\pi q_0} (q_0^2 - 4m_\pi^2)^{3/2} \coth(\beta q_0/4), \quad (2.27)$$

where  $q$  is the momentum of the  $\rho$ -meson, which can be off-shell.

One notices immediately that  $\Pi_L^{(\pi \text{loop})}(q^2) \neq 0$ , as was the case for the quark loop contribution (see Eq. A12). A direct calculation of Figs. 3(c) for  $\Pi_{\mu\nu}^{(\pi \text{tad})}$  would ensure that  $\Pi_L^{(\pi)} = 0$  [25]. We do not do this explicitly here, but evaluate this quantity indirectly assuming the constraint  $\Pi_L^{(\pi \text{loop})}(q^2) \neq 0$ . Since  $\Pi_{\mu\nu}^{(\pi \text{tad})} = \Pi^{(\pi \text{tad})}g_{\mu\nu}$ , it follows that  $\Pi^{(\pi \text{tad})} = -\Pi_L^{(\pi \text{loop})}$ . Thus all polarization functions are known.

#### D. $\rho$ -meson mass and analytic structure of the scattering amplitude

In order to identify the mass of the  $\rho$ -meson, one is required to find the poles of the vector-vector scattering amplitude  $D^{\mu\nu}$  or the corresponding propagator for this channel in the complex energy plane. This translates to finding the poles of the transverse amplitude  $D_T(q^2)$  that is given in Eq.(2.23). We thus investigate the analytic structure of  $D_T$  from Eq.(2.23) in this section.

To avoid the complexity associated with the analytical continuation of the  $\rho\pi\pi$  vertex in the complex plane, we shall assume a constant value for the dimensionless  $\rho\pi\pi$  vertex function  $V_{\rho\pi\pi}$  in the following study of the analytic structure, which is a simplification that will not change the feature of our results.

The poles of the scattering amplitude are given by the zeros of the denominator of  $D_T(q^2)$ , which is, according to Eq. (2.23),

$$F(q) = 1 + 2G_2 \left[ \Pi_T^{(q)}(q^2) + \Pi_T^{(\pi)}(q^2) \right]. \quad (2.28)$$

Before we discuss the analytic structure of the function  $F(q)$ , it is useful to first examine the quark loop contribution  $\Pi_T^{(q)}(q^2)$ . The analytic structure of  $\Pi_T^{(q)}(q^2)$  is governed by the integral  $I_2(q)$ ,

$$iI_2(q) \equiv i \times \frac{i}{\beta} \sum_n e^{i\omega_n \eta} \int^\Lambda \frac{d^3k}{(2\pi)^3} \frac{1}{[k^2 - m_q^2] [(k+q)^2 - m_q^2]}. \quad (2.29)$$

In back-to-back kinematics,  $iI_2$  depends only on the zeroth component of the momentum  $q$ . After evaluating of the Matsubara sum and performing an analytical continuation, one finds the integral in Eq. (2.29) to be

$$iI_2(q_0) = -\frac{1}{2\pi^2} \int_{m_q}^{\Lambda_E} dE \frac{\sqrt{E^2 - m_q^2} \tanh(\beta E/2)}{4E^2 - q_0^2 - i\epsilon}, \quad (2.30)$$

where  $\Lambda_E = \sqrt{\Lambda^2 + m_q^2}$ .

We consider  $iI_2(q_0)$  as a complex function in the complex  $q_0$ -plane. This function has branch points at  $q_0 = \pm 2m_q, \pm 2\Lambda_E$ , but for our purpose only the branch point at  $q_0 = 2m_q$  will be relevant. Choosing in the complex  $q_0$ -plane a cut starting from the branch point  $q_0 = 2m_q$  and running to the right, one has two regions on the first Riemann sheet in which  $iI_2(q_0)$  is to be evaluated separately:

(i) On the first sheet of the complex plane away from the cut, where the integrand in Eq. (2.30) is non-singular,  $iI_2(q_0)$  is readily calculated as

$$iI_2(q_0) = -\frac{1}{2\pi^2} \int_m^{\Lambda_E} dE \frac{\sqrt{E^2 - m_q^2} \tanh(\beta E/2)}{4E^2 - q_0^2}, \quad (2.31)$$

which can be expressed analytically at zero temperature by

$$iI_2(q_0) |_{T=0} = -\frac{1}{8\pi^2} \left[ \ln \frac{\Lambda_E + \Lambda}{m_q} - \frac{\sqrt{4m_q^2 - q_0^2}}{q_0} \arctan \left( \frac{q_0 \Lambda}{\Lambda_E \sqrt{4m_q^2 - q_0^2}} \right) \right]. \quad (2.32)$$

(ii) On the real axis for the values of  $q_0$  with  $2m_q < \text{Re}(q_0) < 2\Lambda_E$ , the integrand of  $iI_2(q_0)$  develops a singularity at  $E = q_0/2$  if  $\epsilon \rightarrow 0^+$ . Making use of the formula

$$\lim_{\epsilon \rightarrow 0^+} \frac{1}{y - i\epsilon} = \mathcal{P} \frac{1}{y} + i\pi \delta(y) \quad (2.33)$$

one obtains

$$iI_2(x) = -\frac{1}{2\pi^2} \mathcal{P} \int_m^{\Lambda_E} dE \frac{\sqrt{E^2 - m_q^2} \tanh(\beta E/2)}{4E^2 - x^2} - \frac{i}{16\pi} \frac{\sqrt{x^2 - 4m_q^2}}{x}, \quad (2.34)$$

where  $\mathcal{P}$  stands for the Cauchy principal value, and  $x$  the real part of  $q_0$ . At zero temperature the integral in Eq. (2.34) can be analytically evaluated as,

$$iI_2(x) |_{T=0} = -\frac{1}{16\pi^2} \left[ 2 \ln \frac{\Lambda_E + \Lambda}{m_q} + \frac{\sqrt{x^2 - 4m_q^2}}{x} \ln \frac{x\Lambda - \Lambda_E \sqrt{x^2 - 4m_q^2}}{x\Lambda + \Lambda_E \sqrt{x^2 - 4m_q^2}} \right] - \frac{i}{16\pi} \frac{\sqrt{x^2 - 4m_q^2}}{x}. \quad (2.35)$$

In order to study poles of the scattering amplitude in the complex plane which are located close to the physical sheet, one has to continue the analytic functions onto the unphysical sheet. The analytic continuation of  $iI_2(q_0)$  through the cut into the second sheet is obtained by [26]

$$iI_2(q_0) |_{2\text{nd}} = iI_2(q_0) |_{1\text{st}} - \frac{1}{8\pi} \frac{\sqrt{4m_q^2 - q_0^2}}{q_0} \tanh\left(\frac{\beta q_0}{4}\right), \quad (2.36)$$

where “1st” and “2nd” denote the first and the second sheet. This analytic continuation is sufficient for our investigation since we are only interested in the poles on the unphysical sheet that is close to the positive real axis of the first sheet.

The integral  $I_2^{(\pi)}$  occurring in the pion loop contribution  $\Pi_T^{(\pi)}(q^2)$  (see Eq. (2.25)) has the same analytic structure as the quark loop integral  $I_2$  discussed above, except that the quark mass  $m_q$  and the hyperbolic tangent in  $I_2$  are replaced in  $I_2^{(\pi)}$  by the pion mass  $m_\pi$  and the hyperbolic cotangent, respectively.

The analytic structure of the function  $F(q)$  in Eq. (2.28), whose zeros correspond to poles of the scattering amplitude, is determined by the integrals  $I_2$  in  $\Pi_T^{(q)}(q^2)$  and  $I_2^{(\pi)}$  in  $\Pi_T^{(\pi)}(q^2)$  which are both two-sheeted functions. Consequently  $F(q)$ , as a combination of  $\Pi_T^{(q)}$  and  $\Pi_T^{(\pi)}$ , has two branches into multi-sheeted functions. In Fig. 4, we illustrate the structure of  $F(q)$  in the complex  $q_0$ -plane:  $F(q)$  has two relevant branch points at  $q_0 = 2m_\pi$ , and at  $q_0 = 2m_q$ , and two branch cuts on the real axis starting from  $2m_\pi$ , and  $2m_q$  respectively and running to the right; A continuous path is drawn to show the joining of Riemann sheets along the branch cuts. We use the notation  $[i^{(q)}, j^{(\pi)}]$  with  $i, j = 1, 2$  to denote different sheets, *e.g.*,  $[1^{(q)}, 2^{(\pi)}]$  stands for the case that  $I_2$  in  $\Pi_T^{(q)}$  takes value on the first sheet, and  $I_2^{(\pi)}$  in  $\Pi_T^{(\pi)}$  on the second sheet, and so on. In order to familiarize the reader with the analytic structure, Fig. 4 shows a path through the multi-sheeted plane: starting from point  $A$  in the plane  $[1^{(q)}, 1^{(\pi)}]$ , crossing the cut into the plane  $[1^{(q)}, 2^{(\pi)}]$ , and following the path until at  $B$  one crosses again a cut into  $[2^{(q)}, 1^{(\pi)}]$ , then turning around to  $C$  and entering into  $[2^{(q)}, 2^{(\pi)}]$ , *etc.*

The numerical evaluation of  $F$  and the ensuing determination of the pole position of  $D_T(q^2)$  for the  $\rho$ -meson mass, is discussed in Sec. IV.

### III. $\pi\pi$ SCATTERING

### A. $s$ -channel $\rho$ -meson exchange

Within the extended NJL model, there are several types of diagrams that contribute to  $\pi\pi$  scattering. The full complement of processes can be found in Ref. [23]. Among these are the box and  $\sigma$  meson exchange diagrams, which dominate the  $s$ -wave scattering and quantitatively reproduce the scattering lengths, but do not suffice to account for the full scattering amplitude as a function of the center of mass energy in the vector-isovector channel [27].

In this work, our interest lies in particular in studying the physical situation in the mid-rapidity region in high energy heavy-ion collisions, where thermal pions are copiously produced with kinetic energy,  $E_\pi \sim 200$  MeV, which is of the order of the typical temperature scale reached by the system shortly after the collisions. At that stage, we expect  $\pi\pi$  scattering to be characterized by a center-of-mass energy  $\sqrt{s} \geq 2E_\pi \sim 400$  MeV. In this energy region, according to the phase shifts data of  $\pi\pi$  scattering [28], the  $\pi\pi$  cross section has already an important contribution from the  $\rho$ -meson exchange channel. Thus, in the following, we shall restrict ourselves to  $\rho$  meson exchange diagrams in the  $s$ -channel which contribute to the  $\pi\pi$  scattering at the lowest order in  $1/N_c$  in the extended NJL model as is shown in Fig. 5. The intermediate  $\rho$ -meson state in this graph is to be understood as being given by the full propagator corresponding to Fig. 3 and this is built up of quark-antiquark excitations as well as  $\pi\pi$  modes. Of all diagrams we evaluate only the  $s$ -channel contribution in Fig. 5, since it should be the dominant contribution to the cross section. The scattering amplitude for this graph is given as

$$-i\mathcal{M}_{\pi\pi \rightarrow \pi\pi} = [-i\Gamma_\mu^{\rho\pi\pi}(-p_2, p_1)f_{\rho\pi\pi}][-iD^{\mu\nu}(p_1 + p_2)][-i\Gamma_\mu^{\rho\pi\pi}(p_4, -p_3)f_{\rho\pi\pi}], \quad (3.1)$$

where  $p_1, p_2$  and  $p_3, p_4$  are the momenta of incoming and outgoing pions, respectively, and  $f_{\rho\pi\pi}$  is the flavor factor to be associated with the  $\rho\pi\pi$  vertex. For example,  $f_{\rho\pi\pi} = 2$  for a  $\rho^0\pi^+\pi^-$  vertex in Fig. 5. At finite temperature, Lorentz covariance is broken, *i.e.*, in general the cross section of a two-body reaction does not only depend on the temperature, but also on the c.m. velocity of the initial pair with respect to the heat bath. In the following calculations we shall assume the initial pion system to be at rest in the heat bath.

Inserting the Lorentz structure of the  $\rho\pi\pi$  vertex given in Eq. (2.20), the scattering amplitude in Eq. (3.1) can then be recast as

$$-i\mathcal{M}_{\pi\pi\rightarrow\pi\pi} = -i[-iV_{\rho\pi\pi}(-p_2, p_1)f_{\rho\pi\pi}]^2 D_T(s)(t-u), \quad (3.2)$$

where  $s$ ,  $t$ , and  $u$  are the standard Mandelstam variables,  $s = (p_1 + p_2)^2$ ,  $t = (p_1 - p_3)^2$ , and  $u = (p_1 - p_4)^2$ . Note that the scattering amplitude is proportional to  $(t-u) = (s - 4m_\pi^2)\cos\theta = (s - 4m_\pi^2)P_1(\cos\theta)$ , which is consistent with the expectation that  $\rho$ -exchange is a  $p$ -wave scattering. Only the transverse component of the  $\rho$ -exchange amplitude contributes to the scattering amplitude due to the specific Lorentz structure of the  $\rho\pi\pi$  vertex and the fact that pions in the initial- and final-state are all on the mass shell. This is in accordance with the fact that the poles of the transverse part of the amplitude  $D_T$  determine the position of the  $\rho$  mass.

The differential cross section follows as

$$\frac{d\sigma(s, t)}{dt} = \frac{1}{16\pi s(s - 4m_\pi^2)} |\mathcal{M}_{\pi\pi\rightarrow\pi\pi}|^2, \quad (3.3)$$

and then the total cross section by

$$\sigma(s) = \int_{t_1}^{t_0} dt \frac{d\sigma(s, t)}{dt} [1 + f_B(\sqrt{s}/2)]^2, \quad (3.4)$$

where  $t_0 = 0$ ,  $t_1 = 4m_\pi^2 - s$ ,  $f_B(x) = 1/[\exp(\beta x) - 1]$ , and the factor  $[1 + f_B(\sqrt{s}/2)]^2$  has been included in order to incorporate the Bose-enhancement effects in the final-state phase space.

## B. Unitarity of the $\rho$ -meson exchange amplitude

Unitarity at zero temperature provides a strong constraint on any scattering calculations, while the situation for finite temperature is less clear. It is thus important to confirm that the choice of diagrams evaluated for the  $\pi\pi$  scattering amplitude lead to a unitary  $S$ -matrix at  $T = 0$ . The  $\pi\pi$  scattering amplitude in our approximation is to be calculated from Eq. (3.2). We note that if  $D_T(q^2)$  is restricted to contain the quark loop contribution  $\Pi_T^{(q)}$  alone, no unitarity condition can be fulfilled as  $\Pi_T^{(q)}$  becomes imaginary only above the  $q\bar{q}$  threshold  $\sqrt{s} \geq 2m_q$ . This threshold is an unphysical artifact of the NJL model, at least in the confined phase. Including the term  $\Pi_T^{(\pi)}$  opens the  $\pi\pi$  threshold for  $\sqrt{s} \geq 2m_\pi$ , and allows the optical theorem to hold for  $\pi\pi$  scattering. We recall once again that, from a physical point of view, this channel is essential, since nearly 100% of the  $\rho$ -mesons decay into pions.



It is apparent from this discussion that  $\pi\pi \rightarrow \pi\pi$  scattering within this model forms part of a coupled channels system that also involves the  $q\bar{q}$  sector. The scattering amplitude for  $\pi\pi \rightarrow \pi\pi$  proceeding via  $\rho$ -meson exchange is only *one* element in the two-channel  $S$ -matrix,

$$S = \begin{pmatrix} S_{q\bar{q} \rightarrow q\bar{q}} & S_{q\bar{q} \rightarrow \pi\pi} \\ S_{\pi\pi \rightarrow q\bar{q}} & S_{\pi\pi \rightarrow \pi\pi} \end{pmatrix}. \quad (3.5)$$

The other channels are all to be understood as proceeding via an  $s$ -channel  $\rho$ -meson exchange, and can be envisaged from Fig. 5(a) by simply constructing the relevant subprocess from this diagram. The matrix elements for the  $q\bar{q} \rightarrow q\bar{q}$  and  $q\bar{q} \leftrightarrow \pi\pi$  are given as

$$-i\mathcal{M}_{q\bar{q} \rightarrow q\bar{q}} = -i[-iV_{\rho q\bar{q}}f_{\rho q\bar{q}}]^2 D_T(s)(t-u), \quad (3.6)$$

and

$$-i\mathcal{M}_{q\bar{q} \rightarrow \pi\pi} = -i[-iV_{\rho q\bar{q}}f_{\rho q\bar{q}}][-iV_{\rho\pi\pi}f_{\rho\pi\pi}]D_T(s)(t-u). \quad (3.7)$$

Thus, noting the explicit form of Eqs.(3.2), (3.6) and (3.7) with  $D_T = 2G_2/F$ , and  $F$  as given in Eq.(2.28), one may factorize each term in the  $S$  matrix as

$$S = \begin{pmatrix} 1 + iA_{q\bar{q}}^2/F & iA_{q\bar{q}}A_{\pi\pi}/F \\ iA_{\pi\pi}A_{q\bar{q}}/F & 1 + iA_{\pi\pi}^2/F \end{pmatrix}. \quad (3.8)$$

In this expression,  $A_{\pi\pi}$  follows directly from Eq.(3.2) to be

$$A_{\pi\pi}^2 = \frac{G_2(s-4m_\pi^2)}{12\pi} \sqrt{\frac{s-4m_\pi^2}{s}} [-iV_{\rho\pi\pi}f_{\rho\pi\pi}]^2, \quad (3.9)$$

while similar arguments can be given to extract  $A_{q\bar{q}}^2$  as

$$A_{q\bar{q}}^2 = \frac{G_2(s-4m_q^2)}{12\pi} \sqrt{\frac{s-4m_q^2}{s}} [-iV_{\rho q\bar{q}}f_{\rho q\bar{q}}]^2. \quad (3.10)$$

Unitarity of the  $S$  matrix,  $SS^+ = 1$ , implies

$$A_{\pi\pi}^2 + A_{q\bar{q}}^2 = -2\text{Im}F = -4G_2\text{Im} \left[ \Pi_T^{(\pi)} \right] - 4G_2\text{Im} \left[ \Pi_T^{(q)} \right]. \quad (3.11)$$

Making use of the explicit result for  $\text{Im} \left[ \Pi_T^{(\pi)} \right]$  from Eqs.(2.27) of the previous section and similar result for  $\text{Im} \left[ \Pi_T^{(q)} \right]$ , one can actually show that  $A_{\pi\pi}^2 = -4G_2\text{Im} \left[ \Pi_T^{(\pi)} \right]$ ,

and  $A_{q\bar{q}}^2 = -4G_2\text{Im}[\Pi_T^{(q)}]$ . Therefore, after including the pion loop contribution to the  $\rho$ -meson exchange amplitude, unitarity can be guaranteed.

For later use, we recall that the elastic cross section in the  $l^{\text{th}}$  partial wave scattering has a unitarity bound:

$$\sigma_l \leq \frac{4\pi(2l+1)}{p_{cm}^2}, \quad (3.12)$$

where  $p_{cm}$  is the c.m. momentum. Since the  $\rho$ -meson exchange corresponds to a  $p$ -wave ( $l = 1$ ) scattering process, the cross section should always be bounded by  $\sigma \leq 12\pi/p_{cm}^2$ .

#### IV. NUMERICAL RESULTS

In this section, we present our numerical results. We first discuss our choice of parameters, which are set at  $T = 0$ . We then discuss the numerical evaluation of the  $\rho$ -meson mass in the complex plane, and the  $\pi\pi$  scattering cross section for a constant value of the  $\rho\pi\pi$  vertex. A complete calculation, including the momentum dependence of the vertex function is presented in the ensuing subsection.

##### A. Parameters

Before discussing our numerical results, we have to specify the four parameters in the present model, namely the current quark mass  $m_0$ , coupling strengths  $G_1$ , and  $G_2$ , and the three-momentum cut-off  $\Lambda$ . Our choice of parameters  $m_0 = 3.7$  MeV,  $\Lambda = 650$  MeV,  $G_1\Lambda^2 = 2.5$ ,  $G_2\Lambda^2 = 2.3$ , leads to a value of the pion mass as  $m_\pi = 140$  MeV, pion decay constant  $f_\pi = 85$  MeV, and quark condensate  $\langle\bar{\psi}\psi\rangle = -(267 \text{ MeV})^3$ , which corresponds to a quark mass  $m_q = 458.2$  MeV at temperature  $T = 0$ . In particular, we have chosen the value of  $G_2\Lambda^2$  in such a way that at  $T = 0$ , the  $\rho$ -meson appears as a  $\pi\pi$  resonance at  $m_\rho \simeq 768$  MeV. The dynamically generated quark mass  $m_q$  resulting from this parameter set is deliberately chosen to be large, so that the  $q\bar{q}$  threshold lies above the physical  $\rho$ -meson position and the  $\rho \rightarrow q\bar{q}$  channel is not open at  $T = 0$ . The value for the condensate  $\langle\bar{\psi}\psi\rangle$  is, however, still acceptable.

## B. $\rho$ -poles and cross section for constant $|V_{\rho\pi\pi}|$

As in Sec. IID, a constant (energy-independent) value of the  $\rho\pi\pi$  vertex function  $|V_{\rho\pi\pi}|$  is used to avoid the intricacies induced by the complicated structure of the  $\rho\pi\pi$  vertex. We have checked this assumption via a direct calculation whose result is shown in Fig. 6. For a rather wide energy range below the  $q\bar{q}$  threshold,  $|V_{\rho\pi\pi}|$  depends only weakly on the energy. In this section, we will assume a constant value of the vertex,  $|V_{\rho\pi\pi}| = 2.4$ .

Fig. 7 shows the energy dependence of different real and imaginary parts of  $F(\sqrt{s})$ , the denominator of the transverse  $\rho$ -meson exchange amplitude  $D_T(s)$  given by Eq. (2.28), at the temperature  $T = 0$ . From this figure, the necessity of including the pion loop contribution  $\Pi_T^{(\pi)}$  into the  $\rho$ -meson self-energy becomes apparent. If there is no pion loop contribution to  $F(\sqrt{s})$ , below the  $q\bar{q}$  threshold  $\sqrt{s} = 2m_q$ , the imaginary part of the quark loop  $\Pi_T^{(q)}$  vanishes, since the decay channel  $\rho \rightarrow q\bar{q}$  is closed, and one finds a real root of  $F(\sqrt{s})$  at  $\sqrt{s} \simeq 620$  MeV where  $1 + 2G_2\text{Re}[\Pi_T^{(q)}] = 0$ . This real  $\rho$ -pole of  $D_T(\sqrt{s})$  corresponds to a  $\rho$ -meson as a  $q\bar{q}$  bound state, and would lead to an unphysical divergence in the  $\pi\pi$  cross section.

If we take the pion loop contribution  $\Pi_T^{(\pi)}$  into account, the imaginary part of the polarization,  $\text{Im}[\Pi_T^{(q)} + \Pi_T^{(\pi)}] \neq 0$  below the  $q\bar{q}$  threshold, as long as it is above the  $\pi\pi$  threshold  $\sqrt{s} = 2m_\pi$ . At the position  $\sqrt{s} \simeq 800$  MeV, where the real part of  $F(\sqrt{s})$  vanishes, the imaginary part of  $F(\sqrt{s})$  does not vanish, and we have to move into the complex energy plane to find a complex root  $m_\rho$  of  $F(q)$ , which corresponds to a  $\rho$ -meson as a  $\pi\pi$  resonance with  $\text{Re}(m_\rho) \simeq 800$  MeV and finite width.

Fig. 8 illustrates  $\rho$ -pole trajectories for different temperatures as a function of the coupling strength  $G_2\Lambda^2$ . At  $T=0$ , for a very large (unphysical) value  $G_2\Lambda^2 = 6.4$ , the  $\rho$ -meson appears as a bound state at 200 MeV and vanishing imaginary part since it is located below the  $\pi\pi$  threshold. With decreasing values of  $G_2\Lambda^2$  the  $\rho$  becomes less bound, until above the  $\pi\pi$  threshold the trajectory moves away from the real axis and  $\text{Im}(m_\rho)$  becomes negative and of the order of 100 MeV. A cross on the trajectory marks the physical value of  $G_2\Lambda^2 = 2.3$ . Decreasing the value of  $G_2\Lambda^2$  even more the trajectory approaches the real axis again, and enters into the sheet  $[2^{(q)}, 1^{(\pi)}]$  closely above the  $q\bar{q}$  threshold. This exercise repeated for several temperatures is shown in Fig. 8. If one follows the position of the crosses, which indicate the physical

location of the  $\rho$  as a function of temperature, one reads off the main result of our investigation: very little changes for  $\text{Re}(m_\rho)$  for temperatures between 0 and 130 MeV. This can be more clearly seen from Fig. 9, where we show the temperature dependence of  $\text{Re}(m_\rho)$ ,  $\text{Re}(m_\pi)$  and  $m_q$ . The pion Mott temperature  $T_M$ , which is defined by  $m_\pi(T_M) = 2m_q(T_M)$ , is found to be  $T_M \simeq 280$  MeV. This somewhat large  $T_M$  is a consequence of the large  $m_q \simeq 460$  MeV at  $T = 0$ .

Fig. 10 shows the cross sections for  $\pi\pi$  scattering, which are calculated for a constant  $|V_{\rho\pi\pi}| = 2.4$ . At  $T = 0$ , we find that the  $\rho$ -pole is located at  $\text{Re}(m_\rho) \simeq 815$  MeV and  $\text{Im}(m_\rho) \simeq -86$  MeV. This  $\rho$ -pole corresponds to the peak of the cross section at  $T = 0$  in Fig. 10 with a width  $\Gamma \sim -2\text{Im}(m_\rho) \sim 170$  MeV. As expected, the cross section at  $T = 0$  touches the unitarity bound. In comparison with the cross section at  $T = 0$ , the peak of the cross section at  $T = 150$  MeV becomes lower, but its position does not shift much. While the cross sections at  $T = 0$  and 150 MeV have resonance-like shapes and can be directly related to the corresponding  $\rho$ -poles given in Fig. 10, the relationship between the  $\rho$ -pole position and the shape of the cross section at  $T = 200$  MeV is less clear. In the latter case, the  $\rho$ -pole on the  $[1^{(q)}, 2^{(\pi)}]$  sheet is found to be slightly above the  $q\bar{q}$  threshold that is indicated in Fig. 8. One may expect in this case, the shape of the cross section is a combination of the effects of the  $q\bar{q}$  threshold and the  $\rho$ -pole we found. On the other hand, the cross section at  $T = 220$  MeV displays mainly the threshold behavior, known in the literature as the Wigner cusp. In this case the  $\rho$ -pole shown in Fig. 8 locates on the  $[2^{(q)}, 1^{(\pi)}]$  sheet, and is so far away from the physical sheet that it cannot make its existence dominant in the shape of the cross section.

### C. Cross sections for energy dependent $|V_{\rho\pi\pi}|$

In our calculations, we have chosen the parameter  $G_2$  so that at  $T = 0$  the  $\rho$ -meson appears as a  $\pi\pi$  resonance with mass  $m_\rho \sim 768$  MeV, as one can see from a fit of the cross section  $\sigma(\pi^+\pi^- \rightarrow \pi^+\pi^-)$  given in Fig. 11 for an energy dependent  $|V_{\rho\pi\pi}|$ . The data points of  $\sigma(\pi^+\pi^- \rightarrow \pi^+\pi^-)$  translated from the phase shifts of  $\pi^+\pi^-$  scattering in the vector-isovector channel [28], instead of the  $\pi^+\pi^-$  total elastic cross section (*e.g.*, given in Ref. [29]), has been used here in order to single out the dominant  $\rho$ -meson exchange contribution to  $\sigma(\pi^+\pi^- \rightarrow \pi^+\pi^-)$

and remove background contributions resulting from other channels that are not present in our calculations. One sees in Fig. 11 that the cross section is properly bounded by the unitarity at  $T = 0$ , and that both the position and the shape can be reasonably reproduced by the present parameter set. Fig. 11 also shows the results for  $\sigma(\pi^+\pi^- \rightarrow \pi^+\pi^-)$  for a constant value of the vertex ( $|V_{\rho\pi\pi}| = 2.4$ ) and for an energy dependent vertex  $|V_{\rho\pi\pi}|$ . The more realistic choice of the energy dependent vertex, with the exception of the area surrounding the  $q\bar{q}$  threshold, gives a better fit to the experimental cross section, which has been calculated from the phase shifts  $\delta_1^1$  for  $\pi\pi$  scattering. The kink on the right hand side of the curve for energy dependent  $|V_{\rho\pi\pi}|$  is due to the opening of the unphysical  $\rho \rightarrow q\bar{q}$  channel.

Fig. 12 illustrates the  $\pi^+\pi^-$  elastic cross sections at different temperatures for energy dependent  $|V_{\rho\pi\pi}|$ , which is entirely determined in Eq. (2.21) by the present model. These results show analogous features to those for a constant  $|V_{\rho\pi\pi}|$  (Fig. 10) in that the position of the maximum moves to smaller values of  $\sqrt{s}$  with increasing temperature. One notes that the height of the maximum decreases with respect to that shown in Fig. 10 for a constant vertex. This is because in this case the cross section is always dominated by  $q\bar{q}$  threshold effects, displaying Wigner cusps.

## V. RESULTS AND CONCLUSIONS

To summarize this work, we have studied the  $\rho$ -meson propagator and  $\pi\pi$  scattering via  $s$ -channel  $\rho$ -meson exchange in the framework of the extended NJL-model. In particular, we have argued that in addition to the quark loop contribution, the  $\rho$ -meson self-energy should include a pion loop contribution from physical considerations which is found to be essential in order to preserve unitarity of the  $S$ -matrix and to reproduce the experimental  $\pi\pi$  phase shifts at zero temperature. In order to maintain current conservation, other diagrams of the same order in  $1/N_c$  expansion must be included. These diagrams reduce to the well-known tadpole diagrams of the hadronic model [6] in the limit in which the quark loops are contracted to a point.

The new part of our work is a careful study of the analytic structure of the two-channel scattering amplitude. We have studied the  $\rho$ -pole trajectories in the twofold cut complex energy plane with respect to the variations of the coupling

strength and temperature. In order to reproduce the data of  $\pi\pi$  phase shifts at zero temperature, it is required that the unphysical  $q\bar{q}$  threshold should be put above the physical  $\rho$  mass, and the  $\rho$ -meson can be consequently identified as a  $\pi\pi$  resonance below the  $q\bar{q}$  threshold. At temperatures  $T < 215$  MeV, the  $\rho$ -meson appears as a complex pole close to the physical sheet. Specifically, as the temperature increases, for temperatures  $T \leq 130$  MeV the  $\rho$ -meson mass increases only slightly and its width is almost unchanged, while for temperatures  $215 \geq T \geq 130$  MeV, both the mass and width of the  $\rho$ -meson decrease. For these temperatures the  $\pi\pi$  cross section has a resonance-like shape, and its temperature dependence is rather weak and is mainly determined by the temperature-dependent  $\rho$ -meson mass and width. At higher temperatures ( $T > 215$  MeV), however, the poles locate on the unphysical sheet and  $q\bar{q}$  threshold effects determine the shape of the cross section. The rather weak dependence of the position and width of the  $\rho$ -pole as a function temperature observed in this work is in agreement with the results of lattice calculations [10].

## ACKNOWLEDGMENTS

We thank the referee for pointing out the importance of current conservation when including the pion contributions to the  $\rho$ -meson polarization functions. This work has been supported in part by the Deutsche Forschungsgemeinschaft DFG under the contract number Hu 233/4-4, and by the German Ministry for Education and Research (BMBF) under contract number 06 HD 742.

## APPENDIX A: ONE-LOOP POLARIZATION FUNCTIONS

In the imaginary time formalism for finite temperature, one loop polarization functions for different meson modes are given by

$$-i\Pi_{\mu\nu,ab}^{VV}(q) = \frac{i}{\beta} \sum_n e^{i\omega_n\eta} \int^\Lambda \frac{d^3k}{(2\pi)^3} (-1) \text{Tr}[(\gamma_\mu\tau_a)iS(k)(\gamma_\nu\tau_b)iS(k+q)], \quad (\text{A1})$$

$$-i\Pi_{ab}^{PP}(q) = \frac{i}{\beta} \sum_n e^{i\omega_n\eta} \int^\Lambda \frac{d^3k}{(2\pi)^3} (-1) \text{Tr}[(i\gamma_5\tau_a)iS(k)(i\gamma_5\tau_b)iS(k+q)], \quad (\text{A2})$$

$$-i\Pi_{\mu,ab}^{PA}(q) = \frac{i}{\beta} \sum_n e^{i\omega_n\eta} \int^\Lambda \frac{d^3k}{(2\pi)^3} (-1) \text{Tr}[(i\gamma_5\tau_a)iS(k)(\gamma_\mu\gamma_5\tau_b)iS(k+q)], \quad (\text{A3})$$

$$-i\Pi_{\mu,ab}^{AP}(q) = \frac{i}{\beta} \sum_n e^{i\omega_n \eta} \int^\Lambda \frac{d^3k}{(2\pi)^3} (-1) \text{Tr}[(\gamma_\mu \gamma_5 \tau_a) iS(k) (i\gamma_5 \tau_b) iS(k+q)], \quad (\text{A4})$$

$$-i\Pi_{\mu\nu,ab}^{AA}(q) = \frac{i}{\beta} \sum_n e^{i\omega_n \eta} \int^\Lambda \frac{d^3k}{(2\pi)^3} (-1) \text{Tr}[(\gamma_\mu \gamma_5 \tau_a) iS(k) (\gamma_\nu \gamma_5 \tau_b) iS(k+q)]. \quad (\text{A5})$$

Here  $\text{Tr}[\dots]$  is a trace over the color, flavor and spinor space,  $\beta$  is the inverse temperature, and the Matsubara sums on  $n$  run over the fermionic frequencies  $\omega_n = (2n+1)\pi/\beta$ , with  $n = 0, \pm 1, \pm 2, \dots$ , which through  $k = (i\omega_n, \mathbf{k})$  enter the quark propagator  $S(k) = (\not{k} + m_q)/(k^2 - m_q^2) = [(i\omega_n)\gamma_0 - \mathbf{k} \cdot \boldsymbol{\gamma} + m_q]/[(i\omega_n)^2 - E_k^2]$ , with  $E_k^2 = \mathbf{k}^2 + m_q^2$ . After performance of the Matsubara summation the limit  $\eta \rightarrow 0$  is to be taken, and an analytic continuation is to be applied to the boson momentum  $q = (i\mu_m, \mathbf{q})$ ,  $\mu_m = 2m\pi/\beta$ ,  $m = 0, \pm 1, \pm 2, \dots$ , which implies  $i\mu_m \rightarrow q_0$ . The three-momentum cut-off  $\Lambda$  is used to regularize the divergences of the integrals.

These polarization functions can be decomposed according to their flavor and spinor structure as,

$$\Pi_{\mu\nu,ab}^{VV}(q^2) = [\Pi_T^{VV}(q)T_{\mu\nu} + \Pi_L^{VV}(q)L_{\mu\nu}] \delta_{ab}, \quad (\text{A6})$$

$$\Pi_{\mu\nu,ab}^{AA}(q^2) = [\Pi_T^{AA}(q^2)T_{\mu\nu} + \Pi_L^{AA}(q^2)L_{\mu\nu}] \delta_{ab}, \quad (\text{A7})$$

$$\Pi_{\mu,ab}^{AP}(q^2) = \Pi^{AP}(q^2) \hat{q}_\mu \delta_{ab}, \quad \hat{q}_\mu = \frac{q_\mu}{\sqrt{q^2}}, \quad (\text{A8})$$

$$\Pi_{ab}^{PP}(q^2) = \Pi^{PP}(q^2) \delta_{ab}, \quad (\text{A9})$$

where the standard longitudinal and transverse tensors are  $L_{\mu\nu} = \hat{q}_\mu \hat{q}_\nu$  and  $T_{\mu\nu} = g_{\mu\nu} - \hat{q}_\mu \hat{q}_\nu$ .

In terms of the following elementary integrals

$$I_1 = \frac{i}{\beta} \sum_n e^{i\omega_n \eta} \int^\Lambda \frac{d^3k}{(2\pi)^3} \frac{1}{k^2 - m_q^2}, \quad (\text{A10a})$$

$$I_2(p) = \frac{i}{\beta} \sum_n e^{i\omega_n \eta} \int^\Lambda \frac{d^3k}{(2\pi)^3} \frac{1}{[k^2 - m_q^2] [(k+p)^2 - m_q^2]}, \quad (\text{A10b})$$

$$I_3(p', p) = \frac{i}{\beta} \sum_n e^{i\omega_n \eta} \int^\Lambda \frac{d^3k}{(2\pi)^3} \frac{1}{(k^2 - m_q^2) [(k+p')^2 - m_q^2] [(k+p)^2 - m_q^2]}, \quad (\text{A10c})$$

one-loop polarization functions can be evaluated as

$$\Pi_T^{VV}(q^2) = \frac{4}{3} i N_f N_c [(q^2 + 2m_q^2) I_2(q) - 2I_1], \quad (\text{A11})$$

$$\Pi_L^{VV}(q^2) = 0, \quad (\text{A12})$$

$$\Pi^{PP}(q^2) = 4i N_f N_c I_1 - 2iq^2 N_f N_c I_2(q), \quad (\text{A13})$$

$$\Pi^{PA}(q^2) = 4m_q N_f N_c I_2(q) / \sqrt{q^2}, \quad (\text{A14})$$

$$\Pi^{AP}(q^2) = -4m_q N_f N_c I_2(q) / \sqrt{q^2}, \quad (\text{A15})$$

$$\Pi_L^{AA}(q^2) = -8im_q^2 N_f N_c I_2(q), \quad (\text{A16})$$

$$\Pi_T^{AA}(q^2) = \Pi_T^{VV}(q^2) + \Pi_L^{AA}(q^2). \quad (\text{A17})$$



## REFERENCES

- [1] H.W. Barz, G. Bertsch, P. Danielewicz and H. Schulz, Phys. Lett. B 275, 19 (1992).
- [2] V. Mull, J. Wambach and J. Speth, Phys. Lett. B 286 (1992) 13 .
- [3] CERES, G. Agakichiev *et al.* , Phys. Rev. Lett. 75, 1272 (1995); HELIOS-3, M. Maser, *et al.* , Nucl. Phys. A 590, 93c (1992).
- [4] C.M. Ko, G.Q. Li, G.E. Brown and H. Sorge, Nucl. Phys. A 610 (1996) 342c.
- [5] C.M. Ko, V. Koch, and G.Q. Li, LBNL-39866, *nucl-th/9702016*.
- [6] C. Gale and J.I. Kapusta, Nucl. Phys. B 357 (1991) 65.
- [7] G.E. Brown and M. Rho, Phys. Rev. Lett. 66 (1991) 2720.
- [8] V.L. Eletsky and B.L. Ioffe, Phys. Rev. D 51, 2371 (1995).
- [9] R.D. Pisarski, Phys. Rev. D 52, R3773 (1995).
- [10] G. Boyd, S. Gupta, F. Karsch, E. Laermann, B. Petersson, and K. Redlich, Phys. Lett. B 349 (1995) 170.
- [11] Y. Nambu and G. Jona-Lasinio, Phys. Rev. 122, 345 (1961); 124, 246 (1961).
- [12] For recent reviews, see *e.g.*, U. Vogl and W. Weise, Prog. Part. Nucl. Phys. 27, 195 (1991); S.P. Klevansky, Rev. Mod. Phys. 64, 649 (1992); T. Hatsuda and T. Kunihiro, Phys. Rep. 247, 221 (1994).
- [13] S. Klimt, M. Lutz, U. Vogl and W. Weise, Nucl. Phys. A 516 (1990) 429; U. Vogl, M. Lutz, S. Klimt and W. Weise, *ibid* 469.
- [14] J. Bijnens, E. de Rafael and H. Zheng, Z. Phys. C64 (1994) 475.
- [15] S. P. Klevansky and R.H. Lemmer, Heidelberg Preprint, HD-TVP-97/05, *hep-ph/9707206*.
- [16] A.H. Blin, B. Hiller and J. da Providência, Phys. Lett. B 241 (1990) 1.
- [17] M. Takizawa, K. Kubodera and F. Myhrer, Phys. Lett. B 261 (1991) 221.

- [18] V. Bernard, A.H. Blin, B. Hiller, Y.P. Ivanov, A.A. Osipov, and U.-G. Meißner, Phys. Lett. B 409 (1997) 483.
- [19] E. Quack and S.P. Klevansky, Phys. Rev. C49, 3283 (1994).
- [20] V. Dmitrašinović, H.-J. Schulze, R. Tegen and R.H. Lemmer, Ann. Phys. (N.Y.) 238 (1995) 332.
- [21] H.-J. Hippe and S.P. Klevansky, Phys. Rev. C52 (1995) 2172.
- [22] M.C. Ruivo, C.A. de Sousa, B. Hiller and A.H. Blin, Nucl. Phys. A575 (1994) 460; H.-J. Schulze, J. Phys. G21 (1995) 185.
- [23] V. Bernard, U.-G. Meißner, A.H. Blin, and B. Hiller, Phys. Lett. B 253 (1991) 443; V. Bernard, A. Blin, B. Hiller, Y.P. Ivanov, A.A. Osipov, and U.-G. Meißner, Ann. Phys. (N.Y.) 249 (1996) 499.
- [24] E. Quack, P. Zhuang, Y. Kalinovsky, S.P. Klevansky, and J. Hüfner, Phys. Lett. B 348 (1995) 1.
- [25] R.H. Lemmer and R. Tegen, Nucl. Phys. A593 (1995) 315.
- [26] J. Hüfner, S.P. Klevansky and P. Rehberg, Nucl. Phys. A606 (1996) 260.
- [27] J. F. Donoghue C. Ramirez and G. Valencia, Phys. Rev. D38, 2195 (1988).
- [28] C.D. Froggatt and J.L. Petersen, Nucl. Phys. B 129 (1977) 89.
- [29] J.P. Baton, G. Laurens and J. Reignier, Phys. Lett. B 33 (1970) 525.

FIGURES

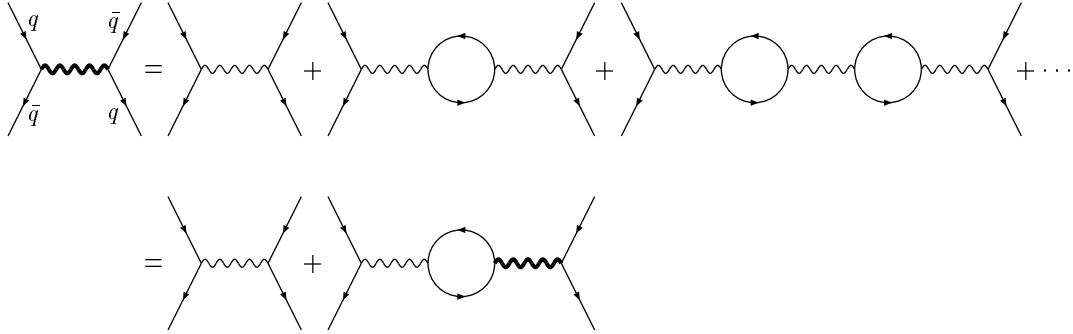


FIG. 1. Quark-antiquark scattering in the random phase approximation, and its recast in the context of the Schwinger-Dyson equation. Thick wavy lines indicate the full propagator of  $\rho$ -meson, and thin wavy lines the bare propagator.

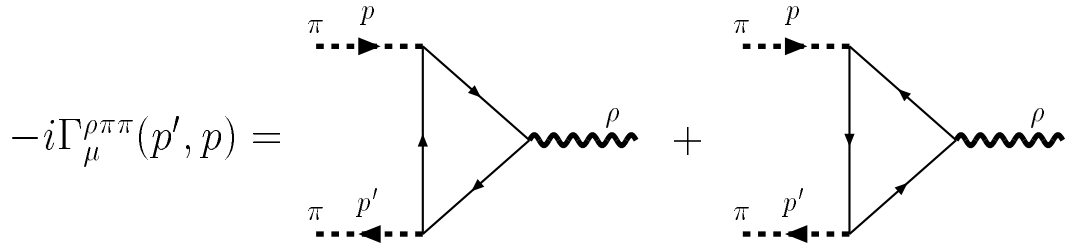


FIG. 2.  $\rho\pi\pi$  vertices to the lowest order in  $1/N_c$ . the two diagrams differ by the direction in the quark loop. They contribute equally as explained in the text.

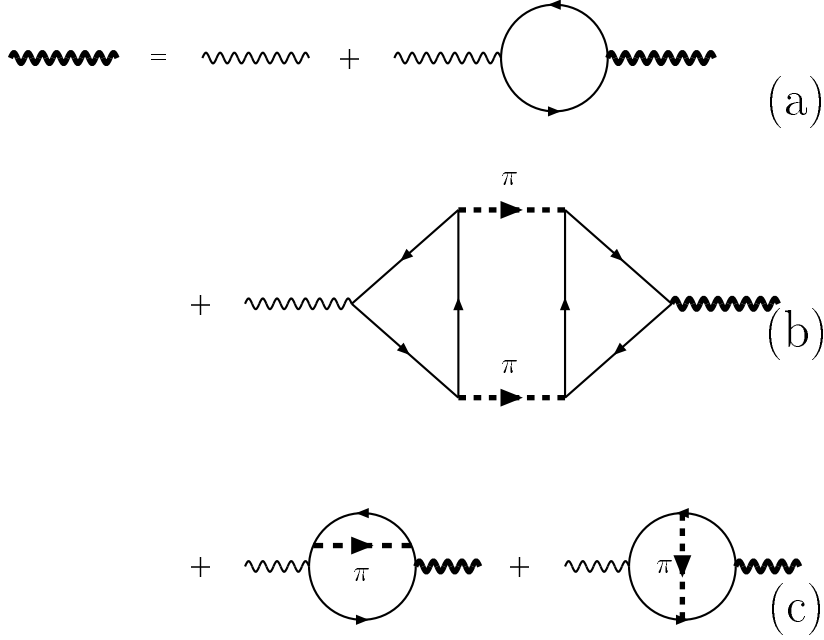


FIG. 3. Quark loop and pion loop contributions to the  $\rho$  propagator: (a) represents the leading order contribution in  $1/N_c$  expansion, while (b) and (c) are the next order corrections. Thick wavy lines indicate the full propagator of  $\rho$ -meson, and thin wavy lines the bare propagator.

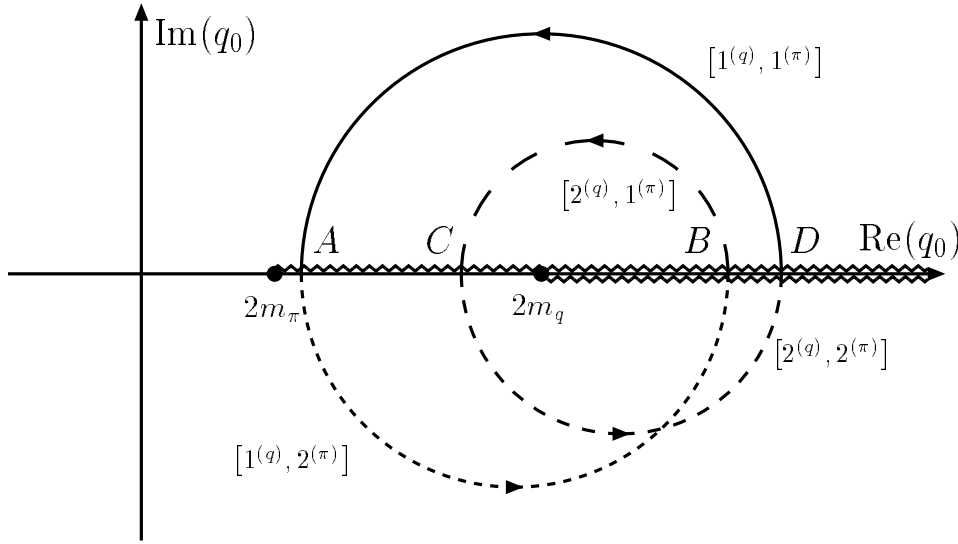


FIG. 4. Joining of Riemann sheets of  $F(q_0)$  along two branch cuts on the real axis starting from thresholds  $2m_\pi$ ,  $2m_q$  and running to the right. Different sheets are denoted by  $[i^{(q)}, j^{(\pi)}]$  with  $i, j = 1, 2$  representing the first, second sheet in  $q\bar{q}$  and  $\pi\pi$  channels, respectively. (see also text.)

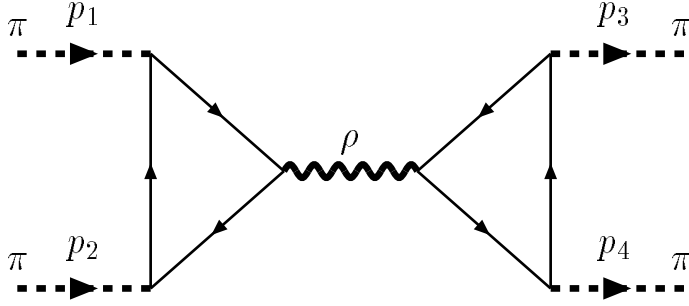


FIG. 5.  $\pi\pi$  scattering via  $s$ -channel  $\rho$ -meson exchange to the lowest order in  $1/N_c$ .

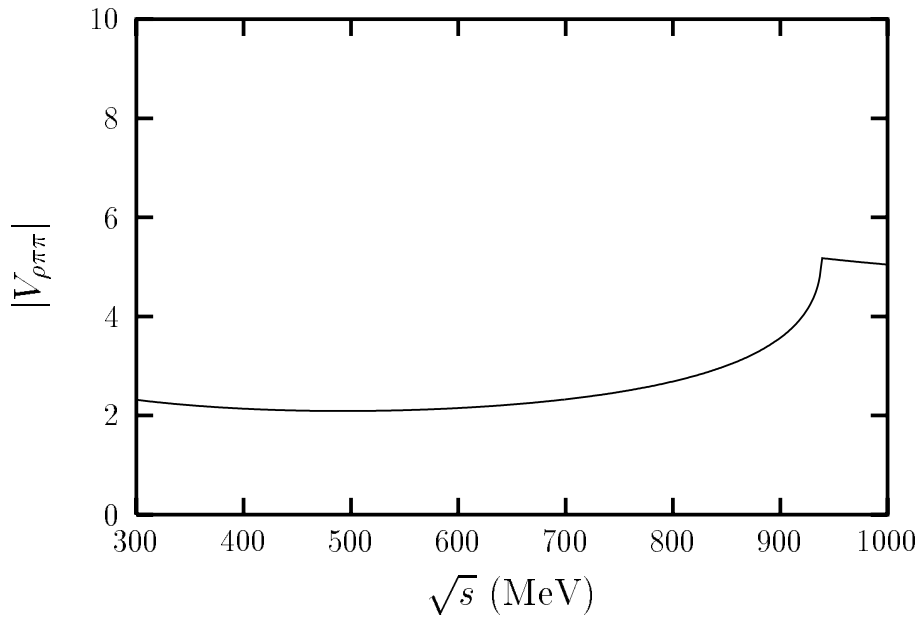


FIG. 6. Energy dependence of the  $\rho\pi\pi$  vertex given by Eq. (2.21) at temperature  $T = 0$ . The discontinuity at  $\sqrt{s} \simeq 920$  MeV relates to the  $q\bar{q}$  threshold  $2m_q$ .

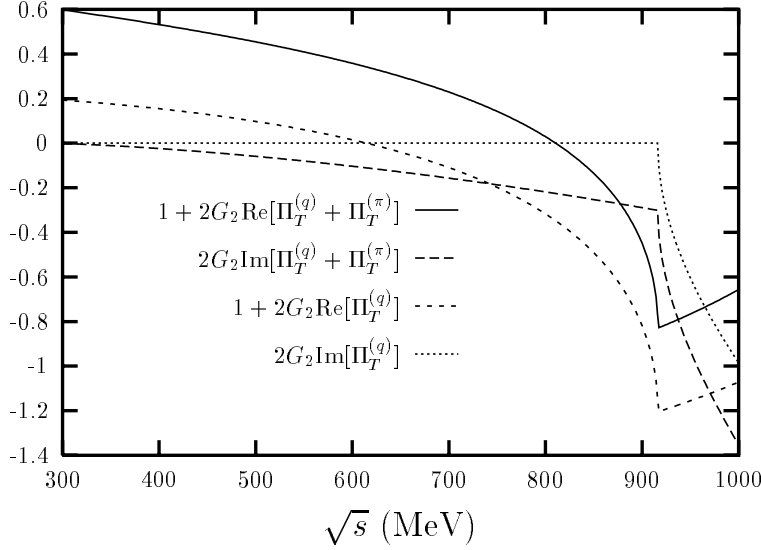


FIG. 7. Energy dependence of real and imaginary parts of the denominator of the  $\rho$ -meson propagator  $F$  in Eq. (2.28) at  $T = 0$ . The breaks at  $\sqrt{s} \simeq 920$  MeV are due to the  $q\bar{q}$  threshold.

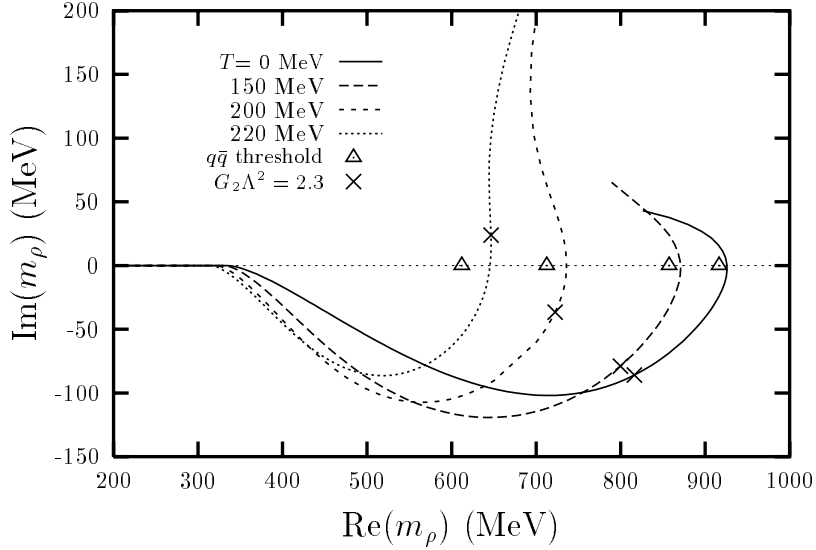


FIG. 8. Variations of the  $\rho$ -pole position in the complex energy plane with the coupling strength  $G_2\Lambda^2$  at different temperatures. The trajectory at  $T = 0$  begins with  $G_2\Lambda^2 = 6.4$  for  $\text{Re}(m_\rho) = 200$  MeV, and it moves to the right with decreasing  $G_2\Lambda^2$ . Similar for other temperatures. For each temperature the  $q\bar{q}$  threshold  $2m_q$  is indicated by a dotted-triangle, and the  $\rho$ -pole position for the physical parameter  $G_2\Lambda^2 = 2.3$  is marked by a cross.

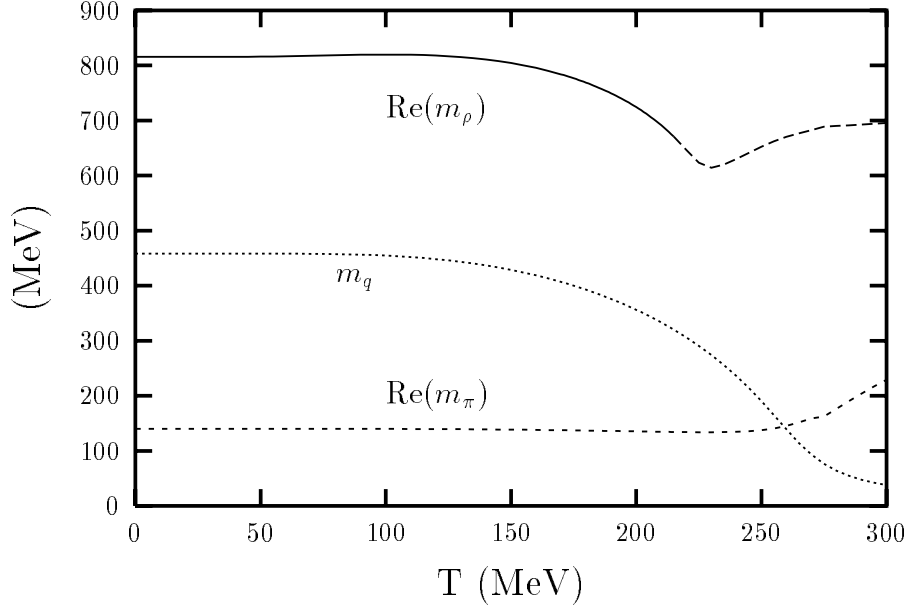


FIG. 9. Temperature dependence of  $\text{Re}(m_\rho)$ ,  $\text{Re}(m_\pi)$ , and  $m_q$ . The long-dashed line indicates the values of  $\text{Re}(m_\rho)$  corresponding to  $\rho$ -poles in the sheet  $[2^{(q)}, 1^{(\pi)}]$ .

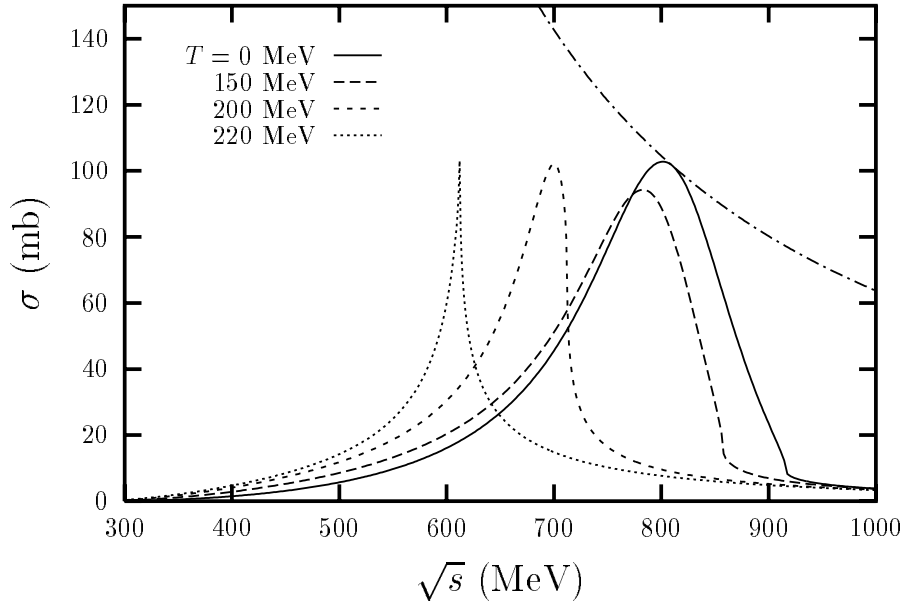


FIG. 10. Calculated  $\pi\pi$  cross sections in the vector-isovector channel at different temperatures for a constant vertex  $|V_{\rho\pi\pi}| = 2.4$ . The unitary bound  $12\pi/p_{cm}^2$  at  $T = 0$  is also shown.

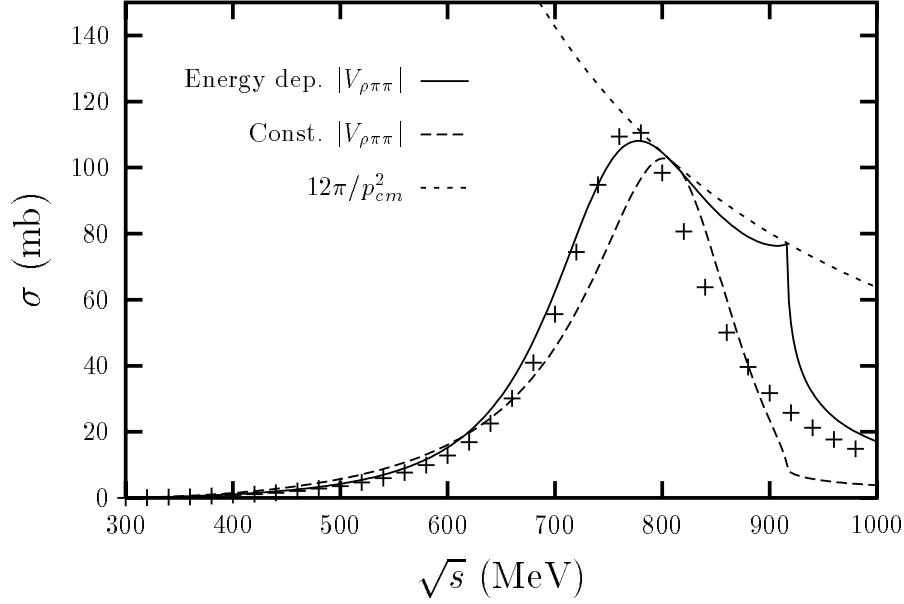


FIG. 11. Energy dependence of the  $\pi\pi$  elastic cross section in the  $\rho$  exchange channel at  $T = 0$  for two choices of the  $\rho\pi\pi$  vertex function (full energy dependence and approximated by a constant), compared to the data (represented by crosses) taken from Ref. [28]. Also shown is the unitary bound  $12\pi/p_{cm}^2$  at  $T = 0$ .

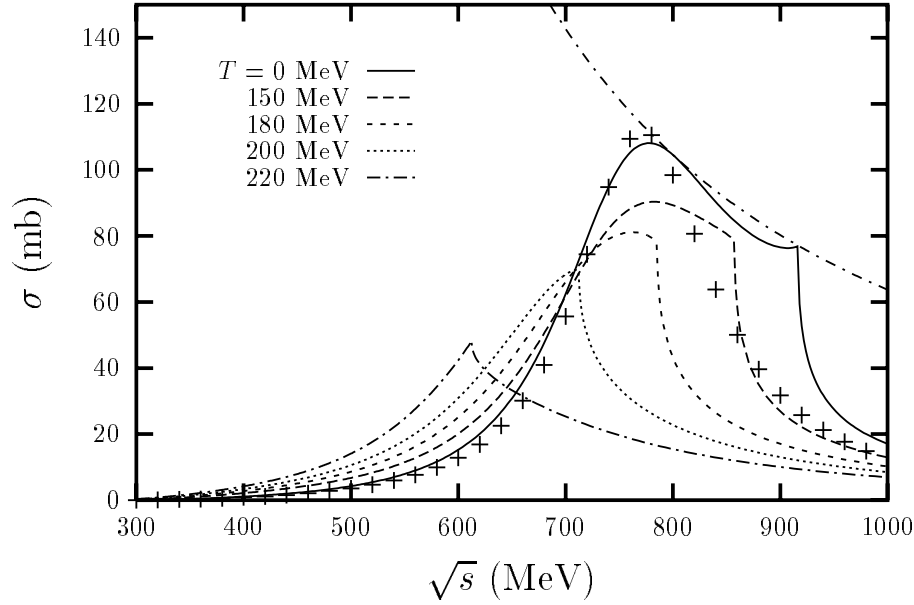


FIG. 12. Elastic  $\sigma(\pi^+\pi^- \rightarrow \pi^+\pi^-)$  at temperatures  $T = 0, 150, 180, 200,$  and  $220$  MeV for energy dependent  $|V_{\rho\pi\pi}|$ . The crosses represent the experimental cross section at  $T = 0$ , and the long dashed line is the unitarity bound  $12\pi/p_{cm}^2$  at  $T = 0$ .